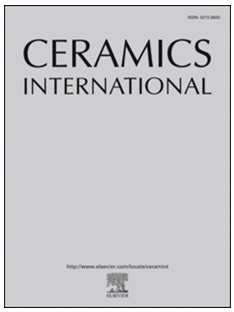

On the physico-mechanical, electrical and dielectric properties of mullite-glass composites

Rivaildo M. Andrade, Allan JM. Araújo, Hugo PA. Alves, João PF. Grilo, Ricardo PS. Dutra, Liszandra FA. Campos, Daniel A. Macedo

PII: S0272-8842(19)31566-4

DOI: https://doi.org/10.1016/j.ceramint.2019.06.070

Reference: CERI 21879

To appear in: *Ceramics International*

Received Date: 21 April 2019

Revised Date: 19 May 2019

Accepted Date: 7 June 2019

Please cite this article as: R.M. Andrade, A.J. Araújo, H.P. Alves, Joã.PF. Grilo, R.P. Dutra, L.F. Campos, D.A. Macedo, On the physico-mechanical, electrical and dielectric properties of mullite-glass composites, *Ceramics International* (2019), doi: https://doi.org/10.1016/j.ceramint.2019.06.070.

On the physico-mechanical, electrical and dielectric properties of mullite-glass composites

Rivaildo M. Andrade[a,*], Allan J. M. Araújo[b], Hugo P. A. Alves[b], João P. F. Grilo[c]
Ricardo P. S. Dutra[a], Liszandra F. A. Campos[a], Daniel A. Macedo[a,*]

[a] Materials Science and Engineering Graduate Program, UFPB, 58051-900 João Pessoa, Brazil
[b] Materials Science and Engineering Graduate Program, UFRN, 59078-970 Natal, Brazil
[c] Department of Materials and Ceramic Engineering, University of Aveiro, 3810-193 Aveiro, Portugal

ABSTRACT

Mullite-glass composites were obtained by solid-state reactive sintering of kaolinite clay and kaolin waste mixtures with waste additions up to 100 wt.%. The structural and microstructural analysis of starting powders and sintered samples were evaluated by X-ray diffractometry (XRD) and field-emission scanning electron microscopy (FESEM). The mechanical properties were evaluated by measuring the flexural strength of sintered bodies. Electrical properties of the composites were assessed by impedance spectroscopy (at 30 ºC and from 400 to 700 °C) in air. A viscous flux mechanism resulting from the glassy phase filled up the open porosity and increased the mechanical strength. Electrical conductivity, dielectric constant and dielectric loss were strongly dependent on the microstructural features, namely glassy phase and porosity. The activation energies (0.89 - 0.99 eV) for electrical conduction were lower than typical literature values of mullite-based materials. The results indicated that the herein synthesized mullite-glass composites with up to 53.6 wt.% mullite are promising low-cost materials for electronics-related applications.

Keywords: Mullite; glassy phase; microstructure; electrical/dielectric properties; impedance spectroscopy.

*Corresponding authors.
E-mail addresses: rivaildomiranda@hotmail.com (Rivaildo M. Andrade), damaced@pq.cnpq.br (Daniel A. Macedo). Tel.: +55 83 32167860 Fax: +55 83 32167906.

Highlights

- Mullite-glass composites from kaolin waste-based formulations.
- Effect of microstructure on properties of mullite-glass composites.
- Electrical and dielectric properties by impedance spectroscopy.
- Low-cost material for electronics-related applications.

1. Introduction

Mullite is one of the most common crystalline phases in ceramic materials. The two main mullite compositions are $3Al_2O_3.2SiO_2$ and $2Al_2O_3.SiO_2$ which are known as mullite 3:2 (stoichiometric mullite) and mullite 2:1, respectively [1,2]. Mullite has been qualified as one of the most important refractory ceramics due to its excellent properties such as low density, high modulus of rupture, good chemical stability, low coefficient of thermal expansion, as well as promising electrical and dielectric properties [3–5]. Stoichiometric mullite has been synthesized by solid-state reaction of synthetic or natural raw materials such as kaolin, alumina, silica, fly ash, and rice husk ash through cationic (Al^{+3} and Si^{+4}) diffusion at temperatures above 1300 °C [4,6–12]. Recently, Foo et al. [13] reported the solid-state synthesis of mullite-based ceramics from coal fly ash and aluminum dross industrial wastes. Another promising raw material to obtain mullite-based composites by reactive sintering is the kaolin waste derived from kaolin processing [14–17]. The use of inorganic wastes is a low-cost and sustainable way to produce a variety of ceramic materials for engineering applications [7,12,18–20].

Mullite and mullite-based composites with low dielectric constant and low losses at high frequencies are suitable for engineering applications such as high-frequency circuit packaging, electronic substrate and ceramic capacitors [5,21]. It is well known that chemical and phase composition, as well as the porosity, strongly affect electrical-dielectric properties of mullite-based materials [5,18,19]. Despite these properties have already been investigated by impedance spectroscopy (IS) [18,19,22], no report was found on the use of IS to study the microstructure-related properties of mullite-glass composites derived from kaolin waste-based compositions. Herein, a comprehensive study of the relationships between phase content, porosity, physico-mechanical, and electrical/dielectric properties of mullite-glass composites is presented

for the first time. Emphasis is dedicated to the use of the impedance spectroscopy technique to determine electrical conductivity and dielectric-related parameters. Mullite-glass composites were obtained by solid-state reactive sintering of mixtures containing kaolinite clay and up to 100 wt.% kaolin waste.

2. Materials and Methods

Starting materials comprising a kaolinite clay and a mica-rich kaolin waste were ball milled in aqueous medium for 5 h using a weight ratio of powder to alumina balls of 1:4. The resulting formulations (waste-free kaolinite clay and up to 100 wt.% kaolin waste addition) were dried at 110 °C for 48 h and sieved (150-mesh). Rectangular ceramic bodies (using 7 wt.% of water as binding agent) (61×21×7.6 mm) and, when convenient, cylindrical samples (Ø 10 mm × 1.5 mm) were shaped by uniaxial pressing at 40 MPa and subsequently fired at 1400 °C for 3 h in air using a heating rate of 3 °C/min.

Particle size distribution and chemical composition of starting powders were obtained by laser diffraction (CILAS 1090, liquid mode) and energy-dispersive X-ray (EDX - Shimadzu, EDX-700), respectively. Mineralogical characterization of raw materials and sintered samples was performed by X-ray di□ractometry (XRD - Shimadzu, XRD 7000, using Cu-Kα, 30 mA and 40 kV). The structural parameters of fired samples were assessed by XRD patterns refinement using the RITA/RISTA routine from the Materials Analysis Using Diffraction (MAUD) software [23,24]. Microstructural characterization of sintered samples (without any posterior surface treatment) was carried out using a field-emission scanning electron microscopy (FESEM, Carl Zeiss, Supra 35-VP Model).

The apparent density and porosity of sintered samples were determined by the Archimedes' principle in distilled water following the relations described in the Eqs. (1) and (2). Total and closed porosity were determined using the relation between open porosity, apparent density and theoretical density. The latter was calculated by the rule of mixtures (using the phase content retrieved by Rietveld analysis of the XRD data) considering theoretical values (from respective ICSD cards) of 3.14, 2.18, 2.36, and 2.65 g/cm^3 for orthorhombic mullite, cristobalite, glass phase, and quartz, respectively. The following Eqs. (3) and (4) were used:

$$\text{Apparent porosity (\%)} = \left(\frac{W_2 - W_1}{W_2 - W_3}\right) \text{ x } 100 \quad (1)$$

$$\text{Apparent density (g/cm}^3\text{)} = \left(\frac{W_1}{W_2 - W_3}\right) x\ \rho_1 \quad (2)$$

$$\text{Total porosity (\%)} = \frac{\text{theoretical density} - \text{apparent density}}{\text{theoretical density}} \text{x} 100 \quad (3)$$

$$\text{Closed porosity (\%)} = \text{total porosity} - \text{open porosity} \quad (4)$$

Where W_1 is the dry weight of the samples, W_2 is the weight of water saturated samples and W_3 is the weight of immersed sample. The density of water is ρ_1 = 1 g/cm³.

The mechanical properties of sintered samples were investigated by using the three-point bending test. The test was performed following ASTM C674. The relation between the modulus of rupture and the applied force (F) is defined in the Eq. (5).

$$\text{Modulus of rupture (MPa)} = \left(\frac{3FL}{2bd^2}\right) \quad (5)$$

Where, L is the length of the support span (mm); b and d are width (mm) and thickness (mm) of the sample, respectively.

Impedance spectroscopy was used to assess the electrical and dielectric properties of mullite-based composites. Measurements were performed from room temperature to 700 ºC under open circuit conditions using a Hewlett Packard 4284A LCR meter in a two-probe configuration (frequency range from 20 Hz to 1 MHz with a voltage amplitude of 0.5 V). Au electrodes were painted on the parallel faces of the samples and thermally treated at 800 °C for 15 min. Electrical conductivity (σ), capacitance (C), dielectric constant (ε_r), and dielectric loss (tanδ) were determined using the following equations (6), (7), (8), and (9):

$$\sigma = \frac{d}{A\,R} \quad (6)$$

$$C = \frac{-i}{(2\,\pi\,f\,Zc)} \quad (7)$$

$$\varepsilon_r = \frac{C\,d}{\varepsilon_0\,A} \quad (8)$$

$$\tan\delta = \frac{\varepsilon}{\varepsilon_r}, \varepsilon = \frac{d}{(2\,\pi\,f)\,A\,\varepsilon_0}\ \frac{Z'}{Z'^2 + Z''^2} \quad (9)$$

Where d and A are the thickness and cross-section area of the ceramic pellet, respectively. R is the total ohmic resistance of the pellet obtained from the impedance spectra by assuming the intercept of the real axis (Z) at low frequency; f is the

frequency in Hz; C is the capacitance in pF; ε_r and ε_0 (8.854×10^{-12} F/m) are the dielectric constant and dielectric permittivity in vacuum, respectively. Z' and $Z''$are the real and imaginary parts of impedance, respectively. The frequency-dependent capacitance was estimated using the equation for the impedance of a capacitor (Eq. 7), considering Zc = Z''. The activation energy for the conduction process (E_a) can be directly calculated from the conductivity values (σ) using the following Arrhenius-type equation (Eq. (10)):

$$\sigma T = \sigma_0 \exp\left(-\frac{E_a}{R T}\right) \quad (10)$$

where σ_0 is a pre-exponential factor, T is the measured temperature (in Kelvin) and R is the gas constant.

3. Results and Discussion

3.1 Microstructural analysis

The diffraction patterns of the starting materials are shown in Fig. 1. Kaolinite clay and kaolin waste have similar phases. The peaks regarding crystalline phases were indexed as kaolinite ($Al_2Si_2O_5(OH)_4$), mica muscovite ($KAl_2Si_3AlO_{10}(OH)_2$) and quartz (SiO_2). Kaolinite is a layered aluminosilicate (1:1) which exhibits a wide range of sintering temperature and mica can act as a fluxing agent at high sintering temperatures. Mineral quartz can increase the mechanical strength during the formation of a liquid phase, functioning as a "skeleton" [25]. According to the rational analysis methodology [26], the phase quantitative content of the starting materials is 67.4, 27.3 and 5.3 wt.% (for the kaolinite clay) and 23.9, 48.7 and 27.4 wt.% (for the waste) of kaolinite, quartz and mica, respectively. The chemical composition of the starting materials is presented in Table 1. The high content of SiO_2 and Al_2O_3 of kaolinite clay and kaolin waste highlights the starting materials as potential candidates to be used in the processing of mullite-based ceramics. The small increment of K_2O in the waste in comparison to kaolinite clay (3.3 *vs.* 0.9 wt.%) may explain the relative higher content of mica in the waste material [25].

Fig. 1. XRD patterns of the starting materials: (a) kaolinite clay and (b) kaolin waste.

Table 1. Chemical composition of the starting materials.

The particle size distribution analysis of the formulations is depicted in Fig. 2. All ceramic formulations exhibit quadrimodal distribution with mean size within 25 – 38 μm. The small deviation on the mean particle size of waste-free clay from the others is explained by the heterogeneity of the waste powder. A wider distribution of powders is usually related to the increase of the packing density of particles. In this sense, smaller particles fit into the gaps of larger particles during the pressing process. This packing improvement is often responsible for increasing densification of sintered ceramics [27]. The concentration of clay minerals (particles < 2 μm) decreased with the addition of kaolin waste. The sand fraction (particles > 20 μm) increased with increasing kaolin waste content. The maximum and minimum values were 69% (100 wt.% kaolin waste) and 42% (waste-free). These results suggest that a further increase in the kaolin waste content leads to formulations with particle sizes comprised in the sand range.

Fig. 2. Particle size distribution of the waste-free clay and samples with up to 100 wt.% kaolin waste content.

XRD patterns of the sintered samples and Rietveld refinement fitting are shown in Fig. 3. Patterns indicate that the obtained ceramics are comprised of crystalline and amorphous phases. XRD patterns of waste-free kaolinite clay and up 30 wt.% waste processed samples (Fig. 3a) were indexed as mullite, β-cristobalite, residual quartz, and a glassy phase indexed as α-cristobalite. The crystallization of β-cristobalite into a α-cristobalite matrix was previously reported in similar materials under identical processing conditions [28]. In addition, attempts in the refinement analysis performed in this work revealed the preferable data fit. Composites with cristobalite phase were obtained from kaolinite clay with high silica content (over 28 wt.% SiO_2, the natural stoichiometric composition) evidenced by the broad peak ($2\boldsymbol{\theta} \approx 22^{o}$) in the patterns. The presence of crystalline cristobalite ($2\boldsymbol{\theta} \approx 22^{o}$) was not observed (Fig. 3b) for the XRD patterns of the sintered samples with the highest waste contents (40 to 100 wt.%). Overall, the retained glassy phase indicates that the mullitization process was not fully reached [29]. The SiO_2-rich phase in the sintered samples is formed after the formation of a liquid phase during the sintering process which is confirmed later in FESEM images [9,30,31].

Fig. 3. Refined XRD patterns of the sintered ceramics: (a) waste-free and up to 30 wt.% waste, (b) 40 to 100 wt.% waste.

The mullite phase lattice parameters and phase composition as a function of added waste content are shown in Fig. 4. Lattice parameters in Fig. 4a remain virtually unchanged with waste additions, in good agreement with the literature [32]. The phase composition as a function of waste content (Fig. 4b) indicates that the waste-free sample is mainly composed of mullite (53.6 wt.%), crystalline cristobalite (assigned as **β**-cristobalite, 28.3 wt.%) and glassy phase (13.8 wt.%). By adding 30 wt.% kaolin waste, crystalline cristobalite decreases to 2 wt.% accompanied by the increase of the glassy phase to 47.9 wt.%, giving rise a mullite-glass composite. As predicted by the SiO_2-Al_2O_3-K_2O phase diagram, K_2O contributes to the formation of a peritectic liquid at temperatures higher than 1140 °C [33]. Therefore, the increase in the amount of glassy phase with increasing the kaolin waste content, depicted in Fig. 4b, would be expected in the current work. The large amount of the glassy phase formed in the kaolin waste processed ceramics, reaching up to 70 wt.%, promotes the dissolution of crystalline silica and, therefore, the content of quartz and cristobalite decreases. On the other hand, mullite content decreases with increasing the kaolin waste content due to excess SiO_2. The presence of residual quartz (< 4.8 wt.%) can be explained by the high silica content of the raw materials and due to its slow dissolution kinetics [31]. The refinement agreement factors were in the ranges: R_{wp} = 7.10 – 14.10%, R_{exp} = 7.51 – 9.64% and χ^2 = 0.92–1.64, and indicate the good quality of the fits.

Fig. 4. (a) Lattice parameters of the mullite phase and (b) phase content (wt.%) as a function of the kaolin waste content, evaluated by Rietveld refinement.

Typical FESEM images of mullite-based composites made with 50 wt.% kaolin waste are shown in Fig. 5. The final sintered body consists mostly of needle-like mullite crystals uniformly embedded into a glassy phase. Energy dispersive spectroscopy (EDS, Fig. 5b) analysis indicates a mullite-glass composite with a potassium aluminosilicate composition, in good accordance with previous works [2,34]. In alumina-silica systems, the formation of mullite phase is generally a consequence of a driving-force promoting dissolution of primary mullite with further precipitation of secondary mullite [35]. In the present work, the presence of alkali oxides impurities (see Table 1) probably

promotes a fluid and corrosive liquid phase responsible for the dissolution of mullite, decreasing the apparent overall mullite content in the resulting sintered sample (Fig. 4b) [29].

Fig. 5. (a) FESEM images and (b) EDS spectrum of a typical mullite-glass composite made with 50 wt.% waste.

3.2 Physico-mechanical properties

Porosity (open and closed) and apparent density of sintered samples as a function of the kaolin waste content are shown in Fig. 6. The open porosity decreased with increasing kaolin waste content, which is ascribed due to the viscous flux mechanism resulting from the glassy phase formation that fills up open pores by capillarity [25,36,37]. The apparent density initially increases for samples with 30 wt.% waste content due to the liquid phase-assisted sintering mechanism. Further reduction of apparent density with increasing kaolin waste content can be explained by the lower density of the glassy phase in comparison to mullite. The negative effect of the closed porosity (sensitive to the glassy phase content) on density will be detailed in the next paragraph.

Closed porosity increases with increasing waste content (Fig. 6a). This fact can be explained by the air expansion in the closed pores as a consequence of the lower viscosity of the glassy phase [25]. An additional drop in the density may also be associated with the increasing of closed pores up to 22.6% for samples with 100 wt.% waste. Clearly, the total porosity increases concomitantly with the closed porosity in waste-processed samples. By adding 50 wt.% waste the total porosity is most likely dominated by the presence of the closed pores (Fig. 6b). Regardless the kaolin waste content, waste addition promotes an increase of the modulus of rupture in comparison to waste-free samples (see Fig. 6c), which is likely associated with the liquid phase assisted-sintering mechanism activated by the increased amount of mica muscovite in waste-processed materials. This mechanism favors a large reduction in apparent porosity and a consequent increase of the mechanical strength.

Fig. 6. (a) Porosity (open, closed and total) and apparent density, (b) FESEM image highlighting closed pores in a mullite-glass composite with 50 wt.% waste and (c) modulus of rupture as a function of the kaolin waste content.

3.3 Electrical and dielectric properties

Impedance spectra of mullite-glass composites obtained in air in the temperature range 400 - 600 °C are shown in Fig. 7. Spectra were corrected using geometric factors (cross-section area of the pellet divided by its thickness). All Nyquist plots show single-arcs slightly depressed without any significant effect of the small tail at lower frequencies, attributed generally to the electrode. Similar impedance spectra have been previously observed for mullite- and cordierite-based composites consisting of crystalline grains embedded into a highly conductive glassy phase [18,19]. In standard impedance spectra of fast oxide-ion conductors, the presence and magnitude of depressed arcs are usually correlated to the contributions of microstructural features (grain and grain boundary). However, correlations between the single semi-arc and the complex microstructure of mullite-glass composites seem to be considerably not obvious. In fact, the separation of contributions in the impedance of biphasic oxide systems is not totally understood, especially when impedance response is composed by simultaneous semi-arcs [38]. Accordingly, in the present work is observed that electrical resistivity decreases with the incorporation of kaolin waste, which is mostly due to the effect of the higher fraction of glassy phase, considered less resistive than mullite [19]. In addition, the presence of alkali oxides into the sintered bodies might promotes distinct conducting mechanism usually efficient to enhance electrical properties [39], but additional proper experiments should be performed to surpass the level of speculation of this additional influence in the resistivity of samples. The resistivity tends to decrease with increasing measuring temperature, as expected for thermally activated processes. The absence of a second impedance arc reflecting the contribution of grain boundaries is consistent with the microstructure (mullite grains embedded into a glassy phase) of the herein studied composites.

Fig. 7. Impedance spectra of mullite-glass composites measured at (a) 400, (b) 500 and (c) 600 °C in air. The numbers indicate the decades of the frequency.

Arrhenius plots of the total electrical conductivity, obtained from the low-frequency intercepts of the impedance spectra with the real axis, are given in Fig. 8. The calculated activation energies (0.89-0.99 eV) are slightly lower than the typical value of mullite-based materials (E_a = 1.2 eV) [19]. The activation energy is a fingerprint of the conducting mechanisms of ceramic samples. The small shift with respect to standard mullite-based ceramics might be attributed to the presence of secondary elements after

the sintering process (e. g. glass, alkali oxides etc.). These elements can impose a relevant feature in the case of mullite-glass composites creating parallels branches, which can modify the usual conducting pathways of species in the presented mullite sintered bodies. Overall, the glassy phase is usually responsible for the conductivity enhancement in glass-containing ceramic systems [19]. Besides, the presence of the glassy liquid phase can mitigate the influence of porosity on the electrical properties by suppression of pores during the sintering process [5,18,19]. Gathering all aspects, it might be reasonable interpret the influence of glassy phase content and porosity on the total conductivity of the presented materials. However, a more detailed inspection with respect of physical properties might indicate the predictable relationships addressed to the further kaolinite clay applications.

Fig. 8. Arrhenius plots of the total conductivity of mullite-glass composites.

Typical capacitance values of 14 pF at 25 Hz and 2.5 pF at 1 MHz were used to calculate the room temperature dielectric constant and dielectric loss as a function of the frequency. The dielectric constant decreased with an increase in frequency and attained 6-7.5 at 1 MHz, regardless of the kaolin waste content (Fig. 9a). At low frequencies, the e□ect on the dielectric constant can be attributed to di□erent types of polarization (electronic, ionic, atomic, and interfacial) and, at the highest frequencies, this e□ect is due to the contribution of electronic polarization [5,40,41]. The dielectric loss also decreased with increasing frequency (Fig. 9b). Dielectric loss values between 0.0004 and 0.001 were found at 1 MHz. These values are considered to be good for electronics-related applications ($\tan\delta < 0.04$) [42]. A further investigation of the sintering temperature effect on the microstructure, physico-mechanical, electrical, and dielectric properties of mullite-glass composites is the topic of forthcoming work.

Fig. 9. (a) Dielectric constant and (b) dielectric loss as a function of the frequency.

4. Conclusions

This work reported the influence of the microstructure on the physical-mechanical, electrical and dielectric properties of mullite-based composites developed

by solid-state reactive sintering of kaolinite clay and mica-rich kaolin waste mixtures. Rietveld analysis confirmed that mullite and glass are the major phases comprising the composites. Lower activation energy for the conduction process (0.89 - 0.99 eV) in comparison to that of typical mullite-based materials, electrical conductivity (1.02×10^{-7} S/cm – 4.49×10^{-7} S/cm at 400 °C), dielectric constant (6 – 7.5 at 1 MHz and 30 °C) and dielectric loss (0.0004 - 0.001 at 1 MHz and 30 °C) values give evidences that the herein synthesized mullite-glass composites with up to 53.6 wt.% mullite (uniformly dispersed into a glass matrix) are promising low-cost materials for electronics-related applications.

Acknowledgments

Financial support from CAPES (Coordenação de Aperfeiçoamento de Nível Superior, Brazil) (Finance Code 001) and CNPq (GDE - 205102/2014-0).

References

[1] W.P. Gonçalves, V.J. Silva, R.R. Menezes, G.A. Neves, H.L. Lira, L.N.L. Santana, Microstructural, physical and mechanical behavior of pastes containing clays and alumina waste, Appl. Clay Sci. 137 (2017) 259–265.

[2] P.J. Sánchez-Soto, D. Eliche-Quesada, S. Martínez-Martínez, E. Garzón-Garzón, L. Pérez-Villarejo, J.M. Rincón, The effect of vitreous phase on mullite and mullite-based ceramic composites from kaolin wastes as by-products of mining, sericite clays and kaolinite, Mater. Lett. 223 (2018) 154–158.

[3] M. Bartsch, B. Saruhan, M. Schmu, H. Schneider, Novel Low-Temperature Processing Route of Dense Mullite Ceramics by Reaction Sintering of Amorphous SiO_2-Coated γ-Al_2O_3, J. Am. Ceram. Soc. 82 (1999) 1388–1392.

[4] H. Schneider, J. Schreuer, B. Hildmann, Structure and properties of mullite-A review, J. Eur. Ceram. Soc. 28 (2008) 329–344.

[5] V.J. da Silva, E.P. de Almeida, W.P. Gonçalves, R.B. da Nóbrega, G. de A. Neves, G. De Araújo, H. de L. Lira, R.R. Menezes, L.N. de L. Santana, Mineralogical and dielectric properties of mullite and cordierite ceramics produced using wastes, Ceram. Int. 45 (2019) 4692–4699.

[6] C. Sadik, I.-E. El Amrani, A. Albizane, Processing and characterization of alumina–mullite ceramics, J. Asian Ceram. Soc. 2 (2014) 310–316.

[7] M.F. Serra, M.S. Conconi, M.R. Gauna, G. Suárez, E.F. Aglietti, N.M. Rendtorff, Mullite ($3Al_2O_3 \cdot 2SiO_2$) ceramics obtained by reaction sintering of rice husk ash and alumina, phase evolution, sintering and microstructure, J. Asian Ceram. Soc. 4 (2016) 61–67.

[8] K.-C. Liu, G. Thomas, A. Caballero, J.S. Moya, S. De Aza, Mullite formation in kaolinite α-alumina, Acta Metall. Mater. 42 (1994) 489–495.

[9] C.Y. Chen, G.S. Lan, W.H. Tuan, Microstructural evolution of mullite during the sintering of kaolin powder compacts, Ceram. Int. 26 (2000) 715–720.

[10] A.E. Souza, S.R. Teixeira, G.T.A. Santos, E. Longo, Addition of sedimentary rock to kaolinitic clays: influence on sintering process, Cerâmica. 59 (2013) 147–155.

[11] İ.A. Aksaf, J.A. Pask, Stable and Metastable Equilibria in the System SiO_2-Al2O_3, J. Am. Ceram. Soc. 58 (1975) 507–512.

[12] Y. Li, J. Feng, Y. Wang, X. Cheng, Preparation of Mullite Ceramics with Fly Ash and Clay by Pickling Process, Int. J. Appl. Ceram. Technol. 12 (2015) E132–E137.

[13] C.T. Foo, M.A.M. Salleh, K.K. Ying, K.A. Matori, Mineralogy and thermal expansion study of mullite-based ceramics synthesized from coal fly ash and aluminum dross industrial wastes Choo, Ceram. Int. 45 (2019) 7488–7494.

[14] R.R. Menezes, M.F. Oliveira, L.N.L. Santana, G.A. Neves, H.C. Ferreira, Utilização do resíduo do beneficiamento do caulim para a produção de corpos mulíticos (Use of kaolin processing waste for the production of mullite bodies), Cerâmica. 53 (2007) 388–395.

[15] R.R. Menezes, M.I. Brasileiro, W.P. Gonçalves, L.N.D.L. Santana, G.A. Neves, H.S. Ferreira, H.C. Ferreira, Statistical Design for Recycling Kaolin Processing Waste in the Manufacturing of Mullite-Based Ceramics, Mater. Res. 12 (2009) 201–209.

[16] M.I. Brasileiro, D.H.S. Oliveira, H.L. Lira, L.N.L. Santana, G.A. Neves, A.P. Novaes, J.M. Sasaki, Mullite preparation from Kaolin residue, Mater. Sci. Forum. 530–531 (2006) 625–630.

[17] M.I. Brasileiro, R.R. Menezes, M.O. Farias, H.L. Lira, G.A. Neves, L.N.L. Santana, Use of kaolin processing waste for the production of mullite bodies, Mater. Sci. Forum. 591–

593 (2008) 799–804.
[18] J.A. Labrincha, C.M. Albuquerque, J.M. Ferreira, M.J. Ribeiro, Electrical characterisation of cordierite bodies containing Al-rich anodising sludge, J. Eur. Ceram. Soc. 26 (2006) 825–830.
[19] M.J. Ribeiro, J.C.C. Abrantes, J.M. Ferreira, J.A. Labrincha, Predicting processing-sintering-related properties of mullite–alumina ceramic bodies based on Al-rich anodising sludge by impedance spectroscopy, J. Eur. Ceram. Soc. 24 (2004) 3841–3848.
[20] R.R. Menezes, H.S. Ferreira, G.A. Neves, H. de L. Lira, H.C. Ferreira, Use of granite sawing wastes in the production of ceramic bricks and tiles, J. Eur. Ceram. Soc. 25 (2005) 1149–1158.
[21] A. Kool, P. Thakur, B. Bagchi, N.A. Hoque, S. Das, Mechanical, dielectric and photoluminescence properties of alumina-mullite composite derived from natural Ganges clay, Appl. Clay Sci. 114 (2015) 349–358.
[22] J.P.F. Grilo, H.P.A. Alves, A.J.M. Araújo, R.M. Andrade, R.P.S. Dutra, D.A. Macedo, Dielectric and electrical properties of a mullite/glass composite from a kaolinite clay/mica-rich kaolin waste mixture, Cerâmica. 65 (2019) 117–121.
[23] H.R. Wenk, S. Matthies, L. Lutterotti, Texture Analysis from Diffraction Spectra, Mater. Sci. Forum. 157–162 (1994) 473–480.
[24] M. Ferrari, L. Lutterotti, Method for the simultaneous determination of anisotropic residual stresses and texture by x□ray diffraction, J. Appl. Phys. 76 (1994) 7246–7255.
[25] H.P.A. Alves, J.B. Silva, L.F.A. Campos, S.M. Torres, R.P.S. Dutra, D.A. Macedo, Preparation of mullite based ceramics from clay–kaolin waste mixtures, Ceram. Int. 42 (2016) 19086–19090.
[26] M.L. Varela, R.M. do Nascimento, A.E. Martinelli, D. Hotza, D.M.A. Melo, M.A.F. Melo, Otimização de uma metodologia para análise mineralógica racional de argilominerais (Otimization of rational mineralogical analysis of ceramics), Cerâmica. 51 (2005) 387–391.
[27] R.K. McGEARY, Mechanical Packing of Spherical Particles, J. Am. Ceram. Soc. 44 (1961) 513–522.
[28] W.M. Kriven, S.-J. Lee, Toughening of mullite/cordierite laminated composites by transformation weakening of β-cristobalite interphases, J. Am. Ceram. Soc. 88 (2005) 1521–1528.
[29] S.C. Vieira, A.S. Ramos, M.T. Vieira, Mullitization kinetics from silica- and alumina-rich wastes, Ceram. Int. 33 (2007) 59–66.
[30] Q. Wei, J. Zhong, Z. Xu, Q. Xu, B. Liu, Microstructure evolution and mechanical properties of ceramic shell moulds for investment casting of turbine blades by selective laser sintering, Ceram. Int. 44 (2018) 12088–12097.
[31] L.N.L. Santana, J. Gomes, R.R. Menezes, G.A. Neves, H.L. Lira, A.M. Segadães, Microstructure development in clays upon heat treatment: Kinetics and equilibrium, Appl. Clay Sci. 135 (2017) 325–332.
[32] H.P.A. Alves, R.A. Junior, L.F.A. Campos, R.P.S. Dutra, J.P.F. Grilo, F.J.A. Loureiro, D.A. Macedo, Structural study of mullite based ceramics derived from a mica-rich kaolin waste, Ceram. Int. 43 (2017) 3919–3922.
[33] E.F. Osborn, A. Muan, Phase Equilibrium Diagrams of Oxide Systems, Am. Ceram. Soc. Edward Orton, Jr., Ceram. Found. Ohio, United States Am. (1960).
[34] W.E. Lee, G.P. Souza, C.J. Mcconville, T. Tarvornpanich, Y. Iqbal, Mullite formation in clays and clay-derived vitreous ceramics, J. Electrochem. Soc. 28 (2008) 465–471.
[35] V. Viswabaskaran, F.D. Gnanam, M. Balasubramanian, Mullitisation behaviour of calcined clay–alumina mixtures, Ceram. Int. 29 (2003) 561–571.
[36] A.A. El-kheshen, M.F. Zawrah, Sinterability, microstructure and properties of glass/ceramic composites, Ceram. Int. 29 (2003) 251–257.
[37] A.J.M. Araújo, H.P.A. Alves, R.M. Andrade, L.F.A. Campos, D.A. Macedo, A.L.S. Pinho, R.M. Nascimento, C.A. Paskocimas, Designing experiments for the optimization of solid-state synthesis and characterization of alumina-based composites, Ceram. Int. 45 (2019) 8525–8532.

[38] J.M. Peko, D.L. Spavieri, L. Charles, C.A. Fortulan, D.P.F. De Souza, M.F. De Souza, Electrical properties of zirconia – alumina composites, Solid State Ionics. 156 (2003) 59–69.

[39] M.J. Ribeiro, D.U. Tulyagavov, J.M. Ferreira, J.A. Labrincha, High temperature mullite dissolution in ceramic bodies derived from Al-rich sludge, J. Eur. Ceram. Soc. 25 (2005) 703–710.

[40] R.R. Heikes, W.D. Johnston, Mechanism of conduction in Li-substituted transition metal oxides, J. Chem. Phys. 26 (1957) 582–587.

[41] S.F. Mansour, Frequency and Composition Dependence on the Dielectric Properties for Mg-Zn Ferrite, Egypt. J. Solids. 28 (2005) 263–273.

[42] L. Zhang, S. Olhero, J.M.F. Ferreira, Thermo-mechanical and high-temperature dielectric properties of cordierite-mullite-alumina ceramics, Ceram. Int. 42 (2016) 16897–16905.

Table caption

Table 1. Chemical composition of the starting materials.

Figure caption

Fig. 1. XRD patterns of the starting materials: (a) kaolinite clay and (b) kaolin waste.

Fig. 2. Particle size distribution of the waste-free clay and samples with up to 100 wt.% kaolin waste content.

Fig. 3. Refined XRD patterns of the sintered ceramics: (a) waste-free and up to 30 wt.% waste, (b) 40 to 100 wt.% waste.

Fig. 4. (a) Lattice parameters of the mullite phase and (b) phase content (wt.%) as a function of the kaolin waste content, evaluated by Rietveld refinement.

Fig. 5. (a) FESEM images and (b) EDS spectrum of a typical mullite-glass composite made with 50 wt.% waste.

Fig. 6. (a) Porosity (open, closed and total) and apparent density, (b) FESEM image highlighting closed pores in a mullite-glass composite with 50 wt.% waste and (c) modulus of rupture as a function of the kaolin waste content.

Fig. 7. Impedance spectra of mullite-glass composites measured at (a) 400, (b) 500 and (c) 600 °C in air. The numbers indicate the decades of the frequency.

Fig. 8. Arrhenius plots of the total conductivity of mullite-glass composites.

Fig. 9. (a) Dielectric constant and (b) dielectric loss as a function of the frequency.

Table 1. Chemical composition of the starting materials.

Oxides	Kaolinite clay (wt.%)	Kaolin waste (wt.%)
SiO_2	65.36	73.27
Al_2O_3	32.48	20.92
K_2O	0.90	3.31
Fe_2O_3	0.90	0.87
Others	0.36	1.63

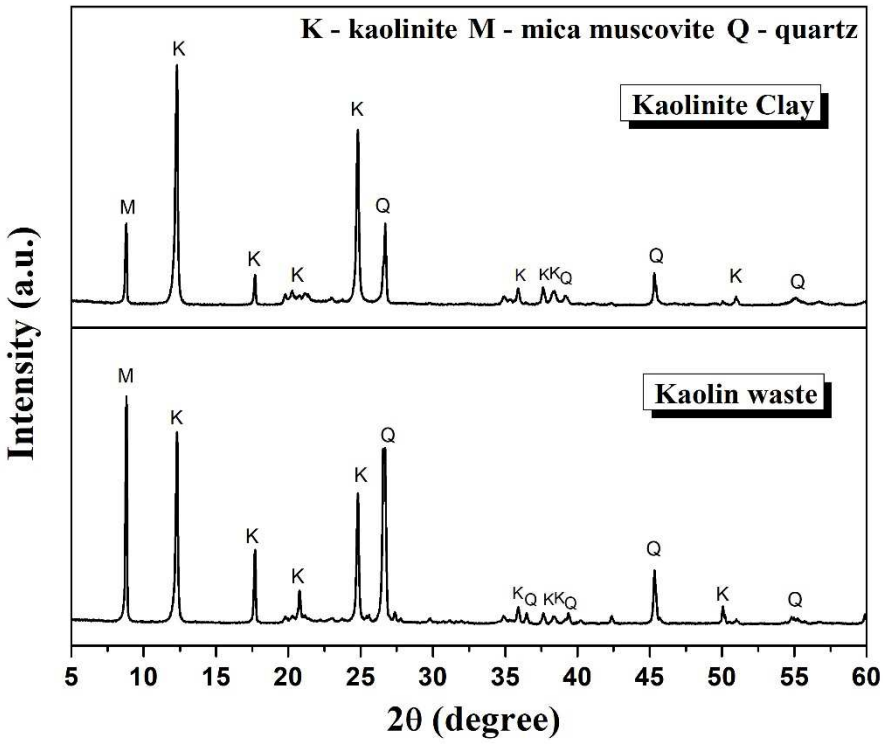

Fig. 1. XRD patterns of the starting materials: (a) kaolinite clay and (b) kaolin waste.

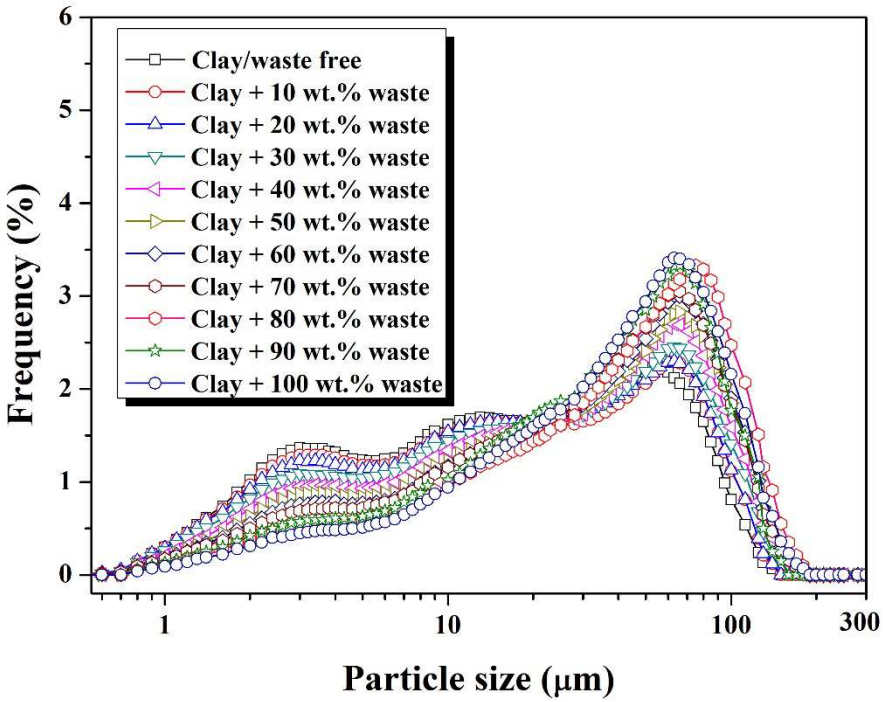

Fig. 2. Particle size distribution of the waste-free clay and samples with up to 100 wt.% kaolin waste content.

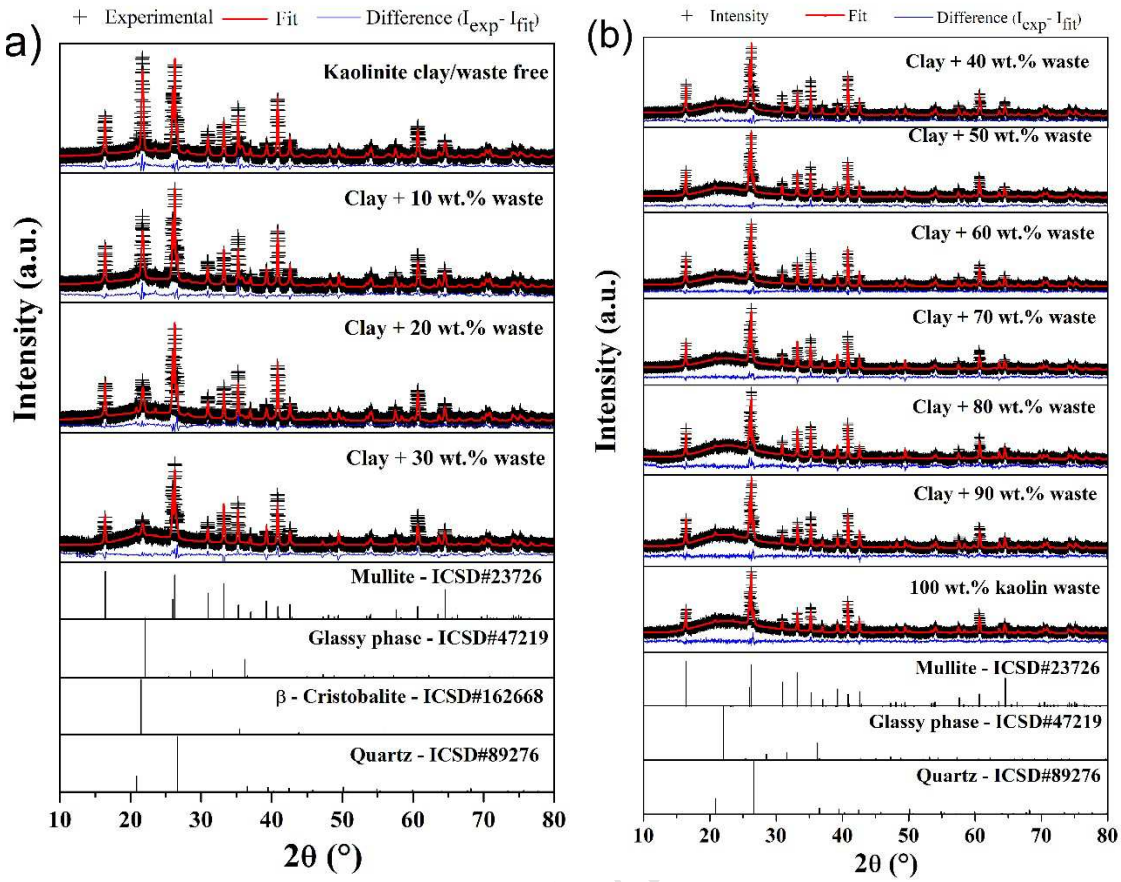

Fig. 3. Refined XRD patterns of the sintered ceramics: (a) waste-free and up to 30 wt.% waste, (b) 40 to 100 wt.% waste.

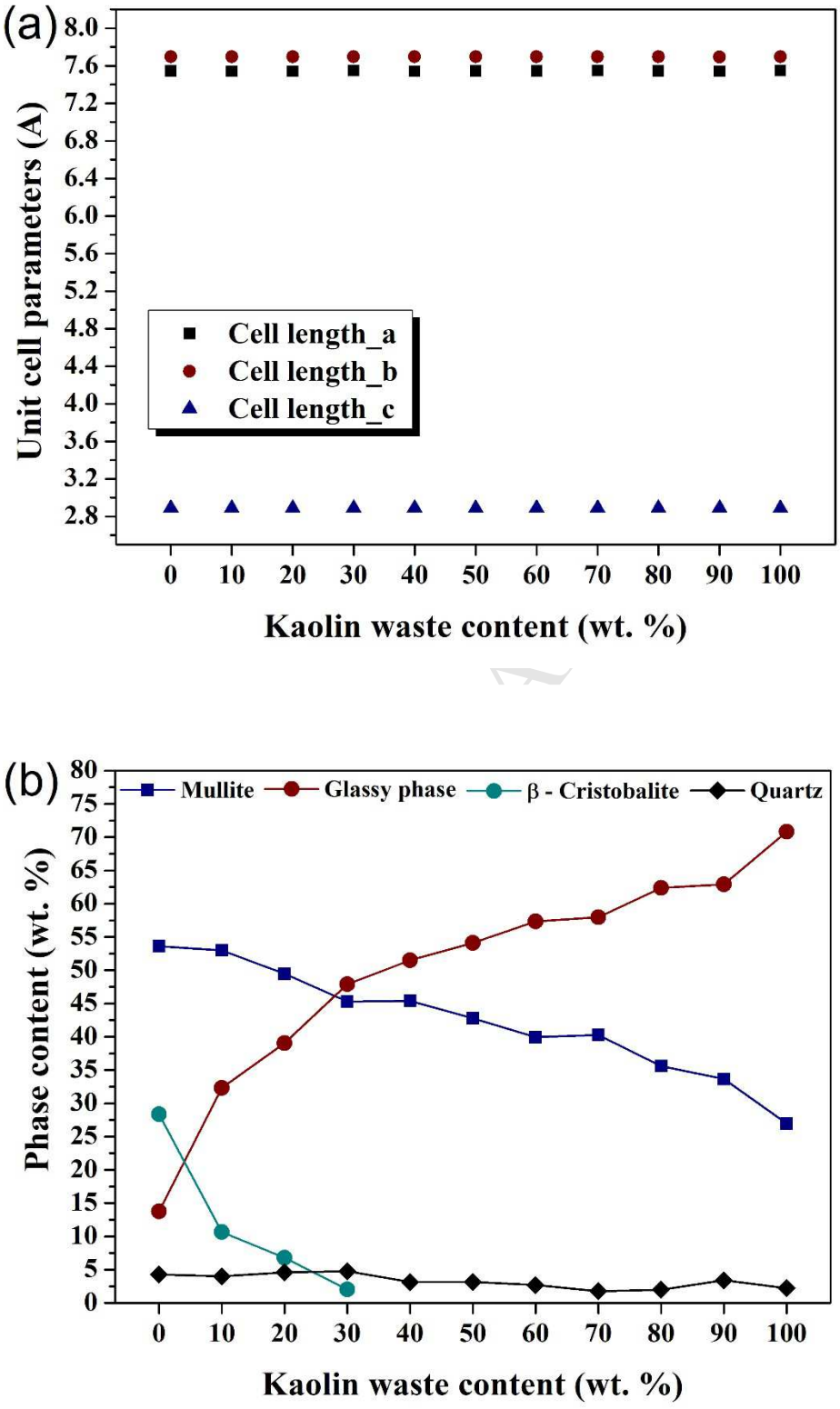

Fig. 4. (a) Lattice parameters of the mullite phase and (b) phase content (wt.%) as a function of the kaolin waste content, evaluated by Rietveld refinement.

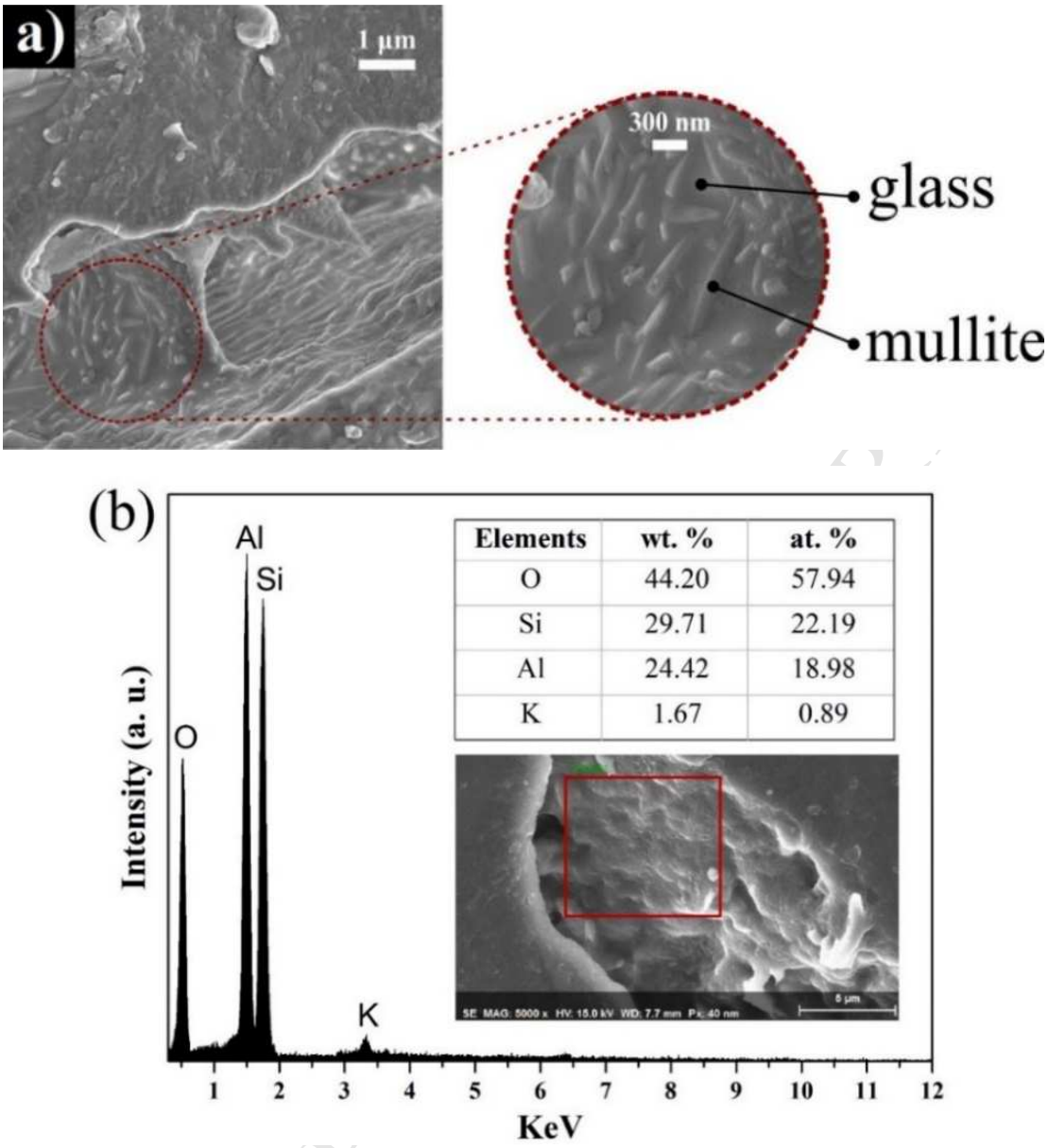

Fig. 5. (a) FESEM images and (b) EDS spectrum of a typical mullite-glass composite made with 50 wt.%.

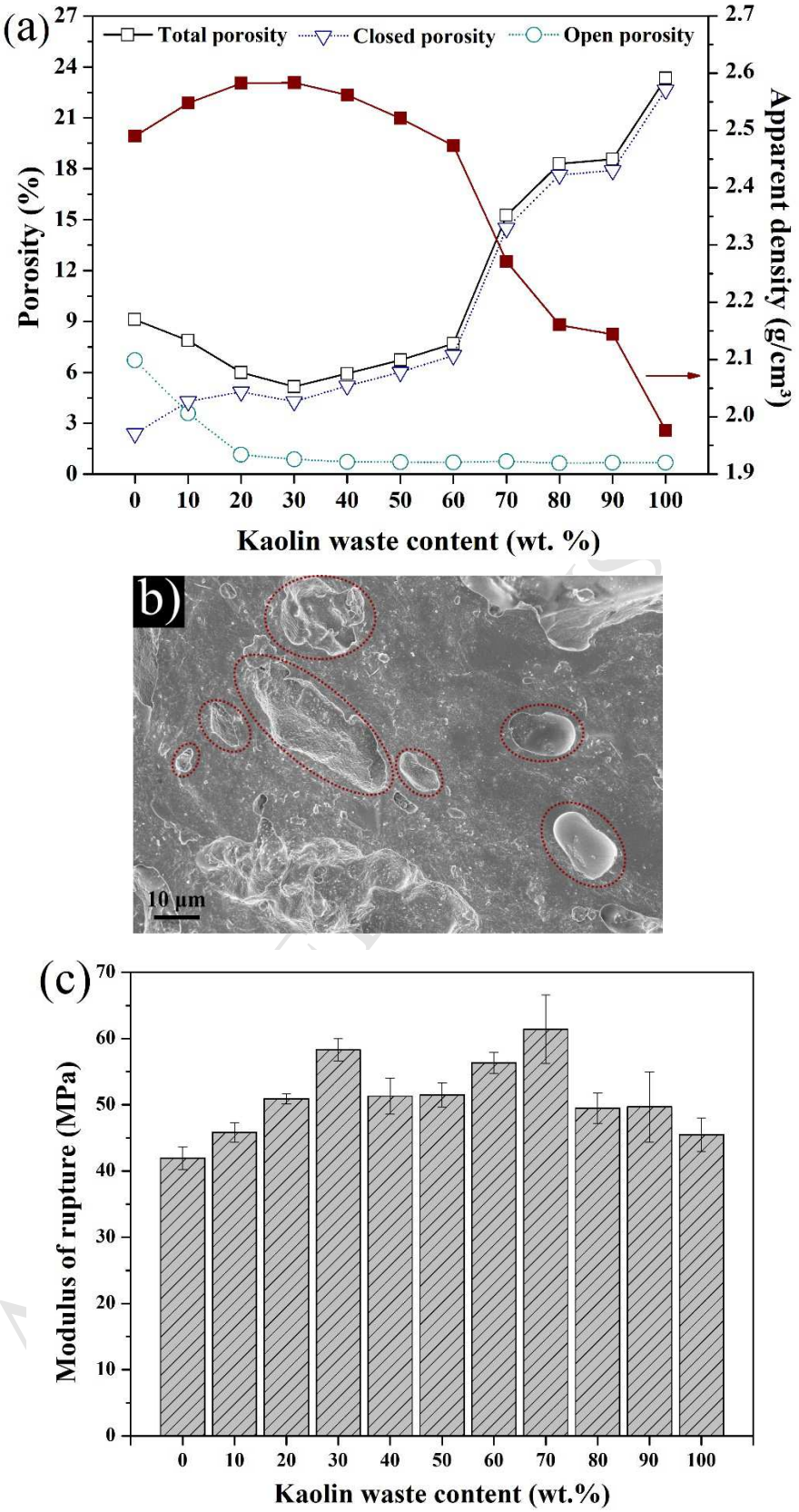

Fig. 6. (a) Porosity (open, closed and total) and apparent density, (b) FESEM image highlighting closed pores in a mullite-glass composite with 50 wt.% waste and (c) modulus of rupture as a function of the kaolin waste content.

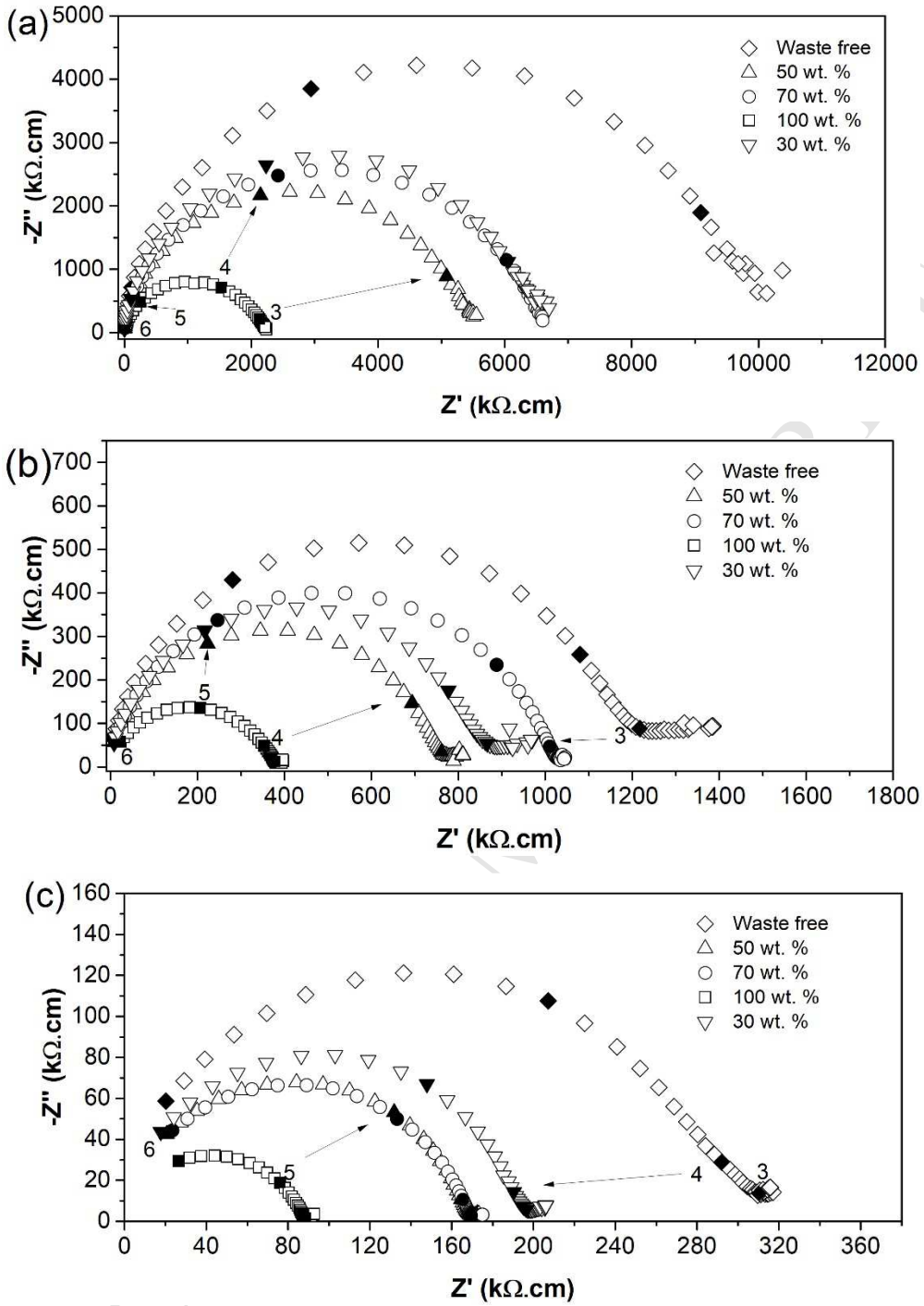

Fig. 7. Impedance spectra of mullite-glass composites measured at (a) 400, (b) 500 and (c) 600 °C in air. The numbers indicate the decades of the frequency.

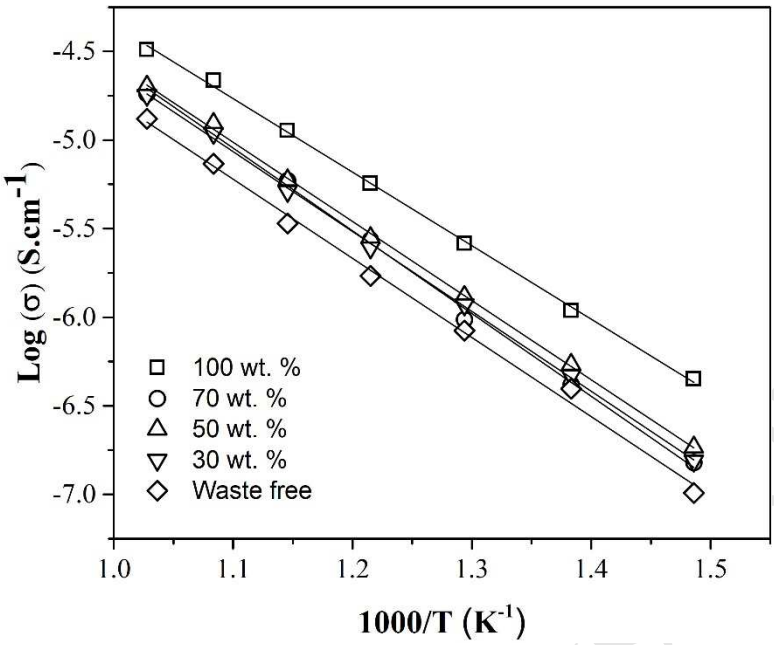

Fig. 8. Arrhenius plots of the total conductivity of mullite-glass composites.

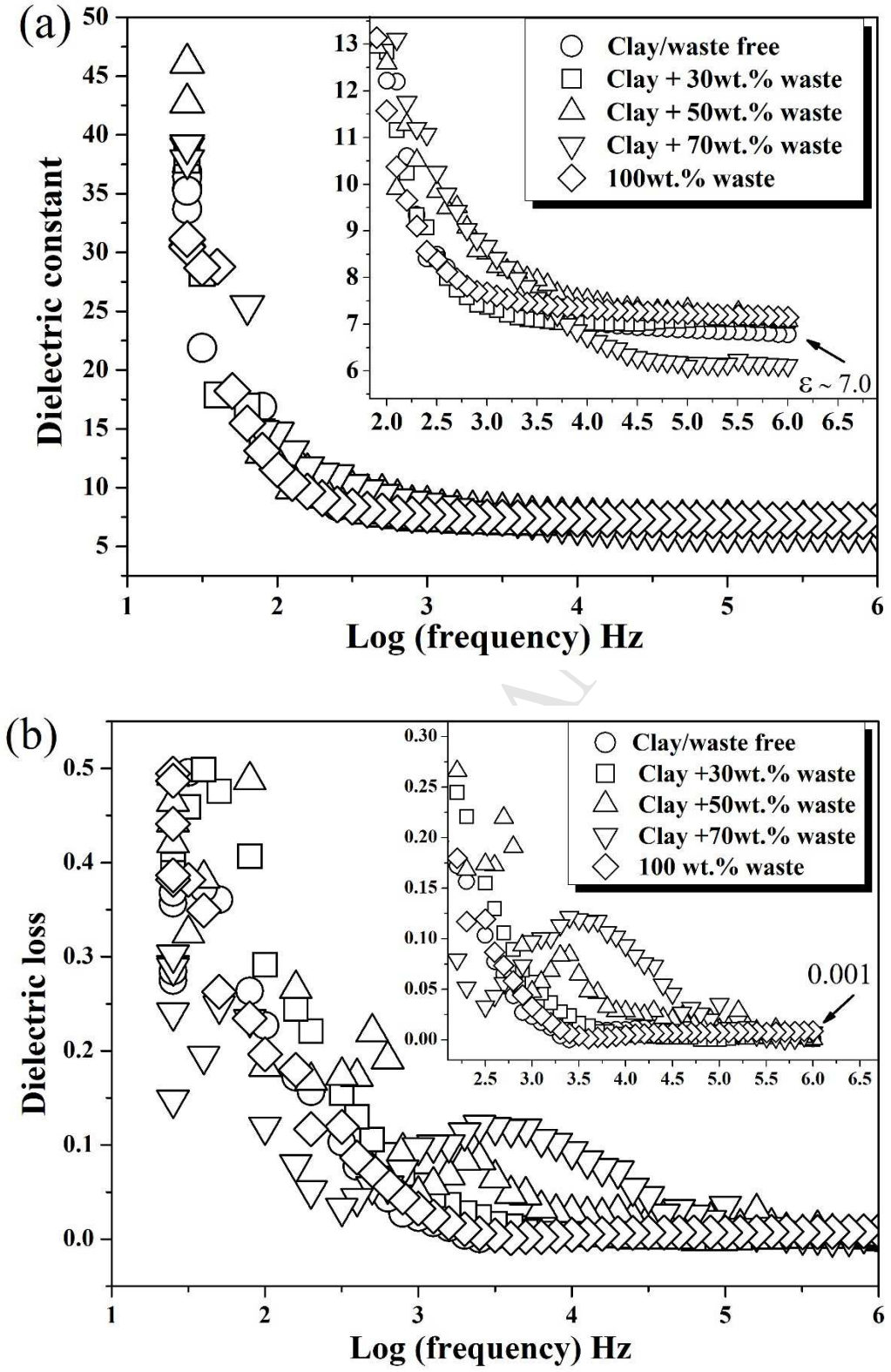

Fig. 9. (a) Dielectric constant and (b) dielectric loss as a function of the frequency.